

Article

MOF-Derived N-Doped C @ CoO/MoC Heterojunction Composite for Efficient Oxygen Reduction Reaction and Long-Life Zn-Air Battery

Ruilian Yin ^{1,2}, Suli Ma ¹, Jiaping Ying ¹, Zhentao Lu ³, Xinxin Niu ⁴, Jinxiu Feng ⁴, Feng Xu ¹, Yifan Zheng ¹, Wenxian Liu ^{4,*} and Xiehong Cao ^{2,4,*}¹ College of Chemical Engineering, Zhejiang University of Technology, Hangzhou 310014, China² Pinghu Institute of Advanced Materials, Zhejiang University of Technology, Jiaxing 314213, China³ College of Information Engineering, Zhejiang University of Technology, Hangzhou 310014, China⁴ College of Materials Science and Engineering, Zhejiang University of Technology, Hangzhou 310014, China

* Correspondence: liuwx@zjut.edu.cn (W.L.); gcscaoxh@zjut.edu.cn (X.C.)

Abstract: The high activity and reliability of bifunctional oxygen catalysts are imperative for rechargeable metal-air batteries. However, the preparation of bifunctional non-noble metal electrocatalysts with multiple active sites remains a great challenge. Herein, an MOF-derived N-doped C-loaded uniformly dispersed CoO/MoC heterojunction catalyst for high-performance dual function was prepared by a simple “codeposition-pyrolysis” method. Experimental investigations revealed that the formation of the heterojunction can tailor the valence of Co and Mo sites, which impressively modulates the electronic properties of the active sites and promotes the electrocatalytic processes. The optimal catalyst reveals a high-wave half potential ($E_{1/2} = 0.841$ V) for ORR and a low overpotential ($E_{10} = 348$ mV) for OER. The NCCM-600-based Zn-air battery displays a high peak power density of 133.36 mW cm⁻² and a prolonged cycling life of more than 650 h. This work provides avenues for the development of functional materials with enhanced properties in a variety of practical energy applications.



Citation: Yin, R.; Ma, S.; Ying, J.; Lu, Z.; Niu, X.; Feng, J.; Xu, F.; Zheng, Y.; Liu, W.; Cao, X. MOF-Derived N-Doped C @ CoO/MoC

Heterojunction Composite for Efficient Oxygen Reduction Reaction and Long-Life Zn-Air Battery.

Batteries **2023**, *9*, 306. <https://doi.org/10.3390/batteries9060306>

Academic Editor: Johan E. ten Elshof

Received: 13 March 2023

Revised: 23 May 2023

Accepted: 28 May 2023

Published: 2 June 2023



Copyright: © 2023 by the authors. Licensee MDPI, Basel, Switzerland. This article is an open access article distributed under the terms and conditions of the Creative Commons Attribution (CC BY) license (<https://creativecommons.org/licenses/by/4.0/>).

Keywords: heterojunction; oxygen reduction reaction; Zn-air battery

1. Introduction

Environmental contamination and the energy crisis have become increasingly severe, which has led to a prioritization of research into energy storage and conversion facilities as potential solutions [1–3]. Rechargeable Zn-air batteries (ZABs) are one of the most concerned devices due to their low cost, high security, and remarkable theoretical energy density (1086 Wh/kg) [4,5]. However, the oxygen evolution reaction (OER) and oxygen reduction reaction (ORR) exhibit complex reaction pathways and sluggish kinetics, which severely hinder the energy utilization of ZABs [6]. Until now, precious metals such as RuO₂ and Pt/C are the most outstanding OER and ORR catalysts, respectively. Nevertheless, their production is limited by scarcity and unsatisfactory durability [7–10]. Therefore, extensive research has been conducted on low-cost yet highly active electrocatalysts to enhance the kinetics of these reactions [11–16].

Recently, transition metals and their compounds have emerged as promising alternative electrocatalysts due to their tunable d-band center, rich electrons in d orbitals, and all kinds of synthesis methods, especially transition metals oxides and carbides [17–20]. For instance, the catalytic performance of single-metal oxides (Co₃O₄, NiO, MnO₂), spinel oxides (NiCo₂O₄, CoFe₂O₄), and TMC nanomaterials (M = W, Mo, Co, V, Fe, Ni, etc.) have been demonstrated in the electrocatalysis of oxygen reaction [21–29]. Unfortunately, these materials are hampered by their low intrinsic activity, undesirable electrical conductivity, and fast degradation [30–33]. In this regard, the construction of heterostructure with synergetic

effects is a proactive activation strategy to boost their catalytic activity, which can not only produce better adsorption/activate the interface of the active substance, but also enable the electron transfer between different components [34–37]. For example, Yang et al. prepared a $\text{Co}_3\text{O}_4/\text{Fe}_3\text{O}_4$ heterostructure catalyst, and its spin–polarization density–functional theory (DFT) and electrocatalytic performance showed that the existence of heterostructures leads to smoother reaction paths and lower overpotentials in the OER process [38]. Additional studies have shown that the heterojunction of $\text{Mo}_2\text{C}/\text{VC}$ with rich active sites not only facilitates electron transfer, but also leads to enhanced desorption kinetics [39]. However, the convenient and controlled preparation processes of heterojunction catalysts remain a thorny challenge [40–44]. Metal–organic frameworks (MOFs) with large specific surface areas, abundant pores, adjustable structures, and controllable compositions are considered promising precursors for the preparation of efficient catalysts with specific structures [45]. In addition, the metal centers in the materials obtained by taking MOFs as precursors are nicely distributed at the atomic level, which is conducive to the formation of heterojunction structures [46–48].

Herein, a rod–like porous N–doped C–loaded CoO/MoC (NCCM) heterojunction catalyst was synthesized by simple pyrolysis of the bimetallic Co/Mo MOF precursor. Due to its high–activity heterojunction sites and one–dimensional porous rod–like structures, NCCM–600 exhibits remarkable bifunctional catalytic activity and reliability towards oxygen electrochemistry, indicating a high–wave half potential ($E_{1/2} = 0.841$ V) for ORR and a low overpotential ($E_{10} = 348$ mV) for OER. Furthermore, the Zn–air battery with NCCM–600 demonstrates a high peak power density of 133.36 mW cm^{-2} and a prolonged cycling life of more than 650 h.

2. Experimental Section

2.1. Material Preparation

2.1.1. Synthesis of Co/Mo MOF

Molybdenum trioxide (5 g), cobaltous nitrate hexahydrate (3.0 g), and imidazole (3.9 g) were dissolved in deionized water (500 mL) and poured into a round–bottom flask. Then, the mixed solution was refluxed at 120 °C for 8 h. The product was centrifuged twice at 6000 rpm, and deionized water was used as a solvent. After drying for 12 h at 60 °C, the Co/Mo MOF was successfully synthesized.

2.1.2. Synthesis of N–Doped Porous C @ CoO/MoC (NCCM) Heterostructure Composite

The Co/Mo MOF (0.5 g) was placed in a quartz crucible. A 0.25 g amount of melamine powder was placed at the upstream side and annealed in a tubular furnace for 2 h at 500 °C, 600 °C, and 700 °C. The obtained 1D N–doped porous C @ CoO/MoC (NCCM) heterostructure composites were named NCCM–500, NCCM–600, and NCCM–700.

2.1.3. Synthesis of Co MOF–Derived CoO

Cobaltous nitrate hexahydrate (3.0 g) and 2–methylimidazole (4.8 g) were dissolved in deionized water (500 mL) and poured into a beaker. Then, the mixed solution was stewed at ordinary temperature for 4 h. The product was centrifuged twice at 6000 rpm, and deionized water was used as a solvent. After drying for 12 h at 60 °C, the Co MOF was successfully synthesized. The as–synthesized Co MOF was annealed for 2 h at 350 °C to acquire MOF–derived CoO.

2.1.4. Synthesis of Mo MOF–Derived MoC

Molybdenum trioxide (5 g) and imidazole (3.9 g) were dissolved in deionized water (500 mL) and poured into a round–bottom flask. Then, the mixed solution was refluxed at 120 °C for 8 h. The product was centrifuged twice at 6000 rpm, and deionized water was used as a solvent. After drying for 12 h at 60 °C, the Mo MOF was successfully synthesized. The as–synthesized Mo MOF was placed in a quartz tube furnace. A 0.25 g amount of

melamine powder was placed at the upstream side and annealed for 2 h at 600 °C to acquire MOF-derived MoC.

2.2. Material Characterization

Powder X-ray Diffraction (PXRD) patterns were recorded on a PANalytical Empyrean powder diffractometer with Cu K α radiation ($\lambda = 0.1541$ nm). The morphology of the prepared samples was revealed by a field-emission scanning electron microscope (FE-SEM, HITACHI Regulus 8100, Tokyo, Japan). The element mappings were analyzed with energy-dispersive X-ray spectroscopy (EDX, Oxford Ultim Max 65, London, UK). The high-resolution nanomorphology was revealed by transmission electron microscopy (TEM, Tecnai G2 F30 S-Twin, Hillsboro, OR, USA) at an accelerating voltage of 200 kV. TX-ray photoelectron spectroscopy (XPS) was conducted on the Kratos AXIS Ultra DLD. The nitrogen adsorption-desorption isotherms and corresponding pore-size distributions were recorded on an automatic physical adsorption instrument (Micromeritics 3Flex, Atlanta, GA, USA).

2.3. Electrochemical Measurement

Electrochemical measurements were made on a conventional three-electrode cell with an RRDE assembly (Pine Research Instrumentation, Durham, NC, USA) and CHI 760E (CH Instruments, Inc., Shanghai, China). The RRDE electrode is composed of a glassy carbon electrode (disk electrode, area: 0.2475 cm²). A graphite rod and saturated calomel electrode (SCE) were used as the counter and reference electrodes, respectively. Catalyst inks were fabricated by mixing 5 mg of catalyst, 30 μ L of Nafion, 200 μ L of ethanol, and 768 μ L of ultrapure water with ultrasonic mixing for 1 h. An 8 μ L volume of the as-obtained suspension was dipped onto the RRDE electrode to form a uniform catalyst layer (the loading of the catalyst was 0.16 mg cm⁻²).

The oxygen reduction reaction (ORR) activity of the different catalysts was evaluated by linear sweep voltammetry (LSV) polarization curves, which were obtained in O₂-saturated 0.1 M KOH at a scan rate of 5 mV s⁻¹ (rotating speed of 1600 rpm). The disk potential ranged from 0 V to 1.0 V (vs. reversible hydrogen electrode (RHE), ERHE = ESCE + 0.244 + 0.059 \times pH). The Koutecky-Levich plots (J^{-1} vs. $\omega^{-1/2}$) were analyzed at various electrode potentials, and the slopes of best-fit lines were used for the calculations. The average number of electrons transferred (n) was calculated using the Koutecky-Levich (K-L) equation in the potential range of 0.4–0.6 V.

$$J^{-1} = J_L^{-1} + J_K^{-1} = (B\omega^{1/2})^{-1} + J_K^{-1}$$

$$B = 0.62nFC_0D^{2/3}\nu^{-1/6}$$

$$J_K = J \times J_L / J_L - J$$

The OER activities of the catalysts were measured by a conventional three-electrode cell at a scan rate of 5 mV s⁻¹ in 1.0 M KOH.

The homemade rechargeable ZAB was assembled according to the configuration. A polished zinc plate and an aqueous solution containing 6 M KOH and 0.2 M zinc acetate were used as anode and electrolyte, respectively. The NCCM heterostructure was dispensed in 1 \times 1 cm⁻² nickel foam as the air cathode. The polarization curves were measured by LSV at 5 mV \cdot s⁻¹ using a CHI 760E electrochemical station, and the power density was calculated from the discharge polarization curve with the following formula:

$$P = VI/S$$

where P is the power density, V is the discharge voltage, I is the discharge current density, and S is the effective catalytic area.

A constant current discharge test (10 mA) was conducted on a NEWARE battery test system, and the specific capacity was calculated from the constant current discharge results and the zinc consumption with the following formula:

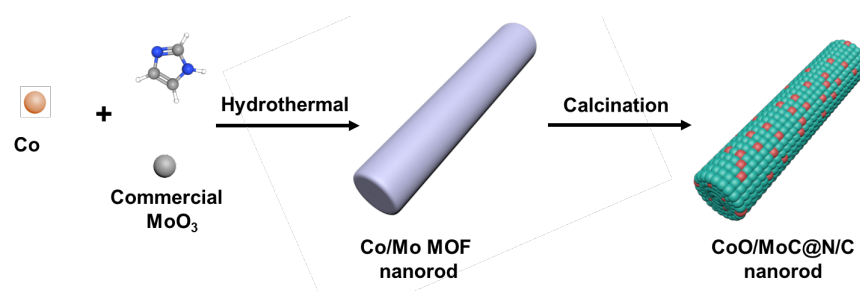
$$SC = TI / \Delta m$$

where SC is the specific capacity, T is the constant current discharge time, I is the discharge current, and Δm is the mass of zinc consumed during the discharge process.

The cycling performance of the ZAB was examined on the NEWARE battery test system at a current density of $10 \text{ mA} \cdot \text{cm}^{-2}$ and charge 30 min–discharge 30 min for one cycle.

3. Results and Discussion

As depicted in Scheme 1, the fabrication process of the N-doped porous C@CoO/MoC (NCCM) is based on a facile “codeposition–pyrolysis” method. Initially, bimetallic Co/Mo MOFs were synthesized through hydrothermal codeposition, and the X-ray diffraction (XRD) pattern of the Co/Mo MOFs exhibited strong and sharp diffraction peaks, indicating excellent crystallinity (Figure S1a, Supporting Information). Subsequently, the NCCM heterojunction was synthesized after pyrolysis of the 1D Co/Mo MOF nanorod with the assistance of melamine at high temperatures under nitrogen atmosphere.



Scheme 1. Schematic of synthesis process for 1D MOF-derived N-doped porous C@CoO/MoC (NCCM).

The morphology of the prepared samples was clearly revealed by scanning electron microscopy (SEM). The obtained Co/Mo MOFs were rod-shaped, with lengths ranging from 5 to 10 μm and diameters ranging from 200 to 400 nm (Figure S1b). Elemental mapping images of the Co/Mo MOF rods confirm the uniform distribution of Co, Mo, C, O, and N elements on the 1D nanorods (Figure S1c). Then, the Co/Mo MOF rods served as self-templates for the synthetic N-doped porous C@CoO/MoC (NCCM) heterojunction composite. After annealing, the nanorods maintained their appearance without collapsing, as shown in Figure 1a. This indicates a complete rod structure with numerous embedded tiny nanoparticles within the graphitized carbon. As the pyrolysis temperature increased, organic ligands decomposed and transformed into graphitic porous carbon. Simultaneously, nitrogen-doped carbon was formed through the decomposition of NH_3 from melamine. Transmission electron microscopy (TEM) images revealed that the NCCM nanorod possesses a porous structure consisting of interconnected nanocrystals encapsulated in N-doped carbon (Figure 1b,c). The pore size is approximately 5 nm, indicating a mesoporous structure that facilitates electrolyte infiltration and reactant diffusion. Moreover, the high-resolution TEM (HRTEM) image of the NCCM presented in Figure 1d reveals that the two distinct lattice stripes are adjacent, with their plane spacing measuring 0.251 and 0.244 nm, respectively, corresponding to the (100) crystal plane of MoC and the (101) crystal plane of CoO. Additionally, as shown in Figure 1e, element mapping analysis of the NCCM nanorod reveals the uniform distribution of Co, Mo, C, O, and N throughout the porous nanorod.

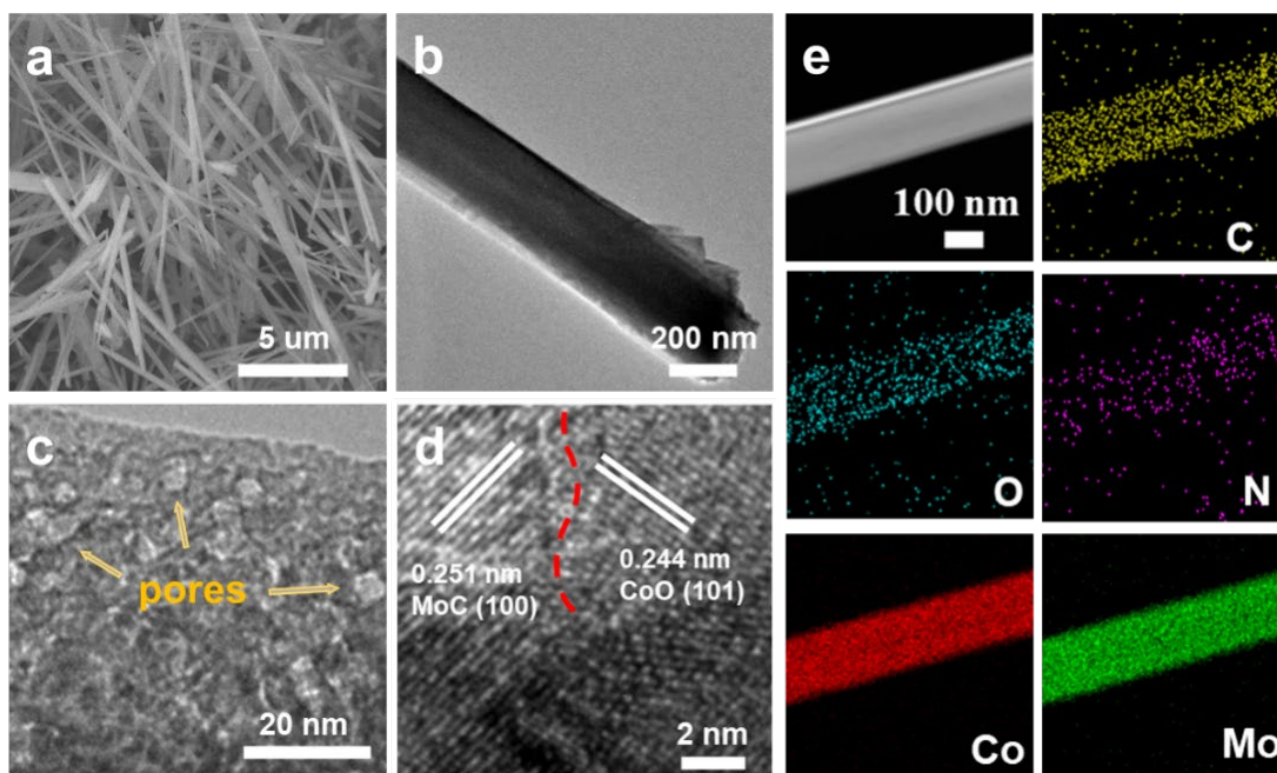


Figure 1. Characterizations of NCCM: (a) SEM images, (b,c) TEM image, (d) HRTEM images, and (e) EDX elemental mapping images.

The formation of the NCCM heterojunction was confirmed through powder X-ray diffraction (PXRD) analyses. Figure 2a displays the PXRD patterns of the NCCM, where all diffraction peaks can be attributed to MoC (JCPDS No. 00–045–1015), CoO (JCPDS No. 01–089–2803), and graphitized C. The chemical structure and coordination environment of the NCCM heterojunction were confirmed by X-ray photoelectron spectroscopy (XPS), which characterizes the composition and valence state of the NCCM. As depicted in Figure 2b, the Co 2p deconvoluted peaks at 781.8 and 798.3 eV in the XPS spectrum are attributed to Co 2p_{3/2} and Co 2p_{1/2}, respectively. Compared to MOF-derived CoO, the binding energy of Co 2p_{3/2} and Co 2p_{1/2} in N-doped porous C@CoO/MoC is positively shifted by 0.9 eV and 1.8 eV, respectively [49]. Similarly, the Mo²⁺, Mo⁴⁺, and Mo⁶⁺ peaks in N-doped porous C@CoO/MoC are positively shifted by 0.4, 0.3, and 2.2 eV with respect to MOF-derived MoC [50] (Figure 2c). These results suggest that the electronic structure of the N-doped porous C@CoO/MoC heterojunction is synergistically regulated. As shown in Figure 2d–f, the O 1s peaks located at approximately 530.3, 531.2, and 532.8 eV and the two peaks at 530.3 and 532.8 eV further confirm the successful formation of CoO, and the peak at 531.2 eV corresponds to –C–O–C– [40]. The C 1s peaks located at about 284.4, 285.1, 286.3, and 288.8 eV might correspond to the Mo–C, C–C, C–O, C=O, and O–C=O bonds, respectively [51]. The N 1s peaks observed at approximately 401.5, 400.1 eV, and 398.5 eV were assigned to graphitic N, pyrrolic–N, and pyridinic–N, respectively. These findings imply that the coordination environment of Co and Mo can be tailored through heterojunction formation, which effectively modulates the electronic structure of the active site, thereby facilitating electrocatalysis.

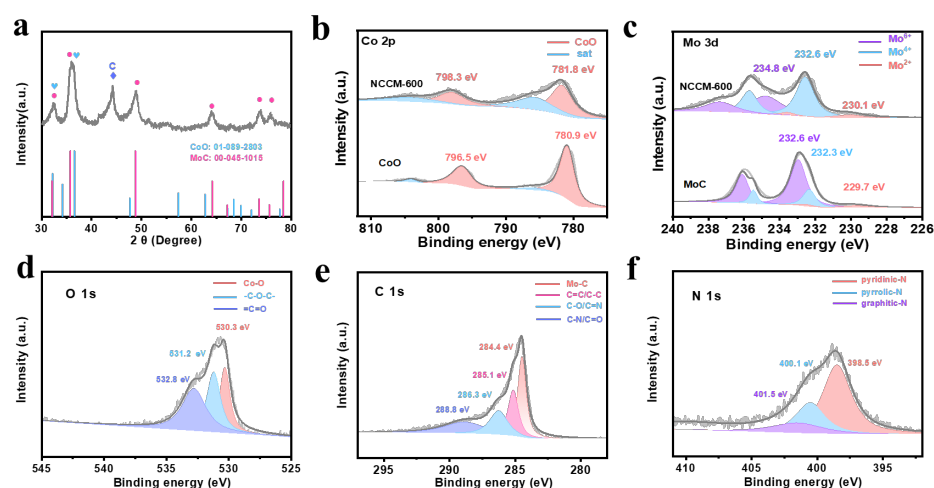


Figure 2. (a) PXRD patterns of NCCM and (b–f) X-ray photoelectron spectroscopy results of NCCM.

The specific surface area of a catalyst is a crucial indicator for evaluating its performance. Therefore, nitrogen isothermal adsorption–desorption curves and specific surface area were characterized for different catalysts. Figure S4 demonstrates that all catalysts exhibit a type-IV isotherm, suggesting the existence of mesopores. NCCM-600 is composed of N-doped carbon-coated interconnected nanocrystals with a more obvious hysteresis, indicating the presence of additional mesoporous pores, which is consistent with the TEM results. The specific surface areas of MOF-derived N-doped porous C@CoO/MoC, MOF-derived CoO, and MOF-derived MoC are $137.92 \text{ m}^2 \cdot \text{g}^{-1}$, $35.63 \text{ m}^2 \cdot \text{g}^{-1}$, and $23.43 \text{ m}^2 \cdot \text{g}^{-1}$, respectively. The significant increase in specific surface area facilitates faster ion diffusion in the electrolyte and the efficient transport of reactive species, thereby effectively enhancing electrocatalysis.

To elucidate the structural advantages of the MOF-derived N-doped porous C@CoO/MoC heterojunction composite in electrocatalysis, we investigated the ORR performance of these catalysts on a rotating disk electrode (RDE) in a 0.1 M KOH solution. The cyclic voltammetry (CV) curves of the NCCM were compared in the N_2 - and O_2 -saturated electrolyte, with Figure S5 showing a distinct cathodic peak at 0.84 V in the O_2 -saturated electrolyte, indicating the remarkable ORR performance of NCCM-600. The ORR activity of the as-synthesized catalysts was then confirmed by linear sweep voltammetry (LSV) at 1600 rpm. As presented in Figure 3a, NCCM-600 exhibits the preferable ORR activity with an onset potential (E_0) of 0.941 V and a half-wave potential ($E_{1/2}$) of 0.841 V, which are higher than those of MoC ($E_0 = 0.823 \text{ V}$, $E_{1/2} = 0.718 \text{ V}$), CoO ($E_0 = 0.761 \text{ V}$, $E_{1/2} = 0.622 \text{ V}$), NCCM-500 ($E_0 = 0.723 \text{ V}$, $E_{1/2} = 0.617 \text{ V}$), and NCCM-700 ($E_0 = 0.886 \text{ V}$, $E_{1/2} = 0.822 \text{ V}$) and approach to Pt/C ($E_0 = 0.990 \text{ V}$, $E_{1/2} = 0.875 \text{ V}$). The Tafel slope of NCCM-600 was the smallest (63.4 mV dec^{-1}) of all the catalysts, manifesting superior ORR kinetics (Figure 3b). Additionally, the kinetic parameters of the NCCM were studied by the LSV curves at seven different rotation rates (Figure 3c,d), corresponding to the Koutecky–Levich (K–L) curves. The calculated electron transfer number (n) is about 4 for NCCM-600, confirming the four-electron ORR route for the catalytic process. In addition to catalytic activity, its stability is also an essential parameter to evaluate the actual performance of the catalyst. As shown in Figure 3e,f, after the introduction of methanol at 400 s, the ORR relative current density of commercial Pt/C catalysts decreases rapidly, whereas the performance of NCCM-600 remains virtually unchanged, demonstrating that NCCM-600 possesses enhanced tolerance against methanol poisoning. Moreover, NCCM-600 maintained 91% of its current density after 24 h of continuous operation, whereas Pt/C had significant degradation with only 81% retention, indicating the better durability of NCCM-600 over the Pt/C catalyst.

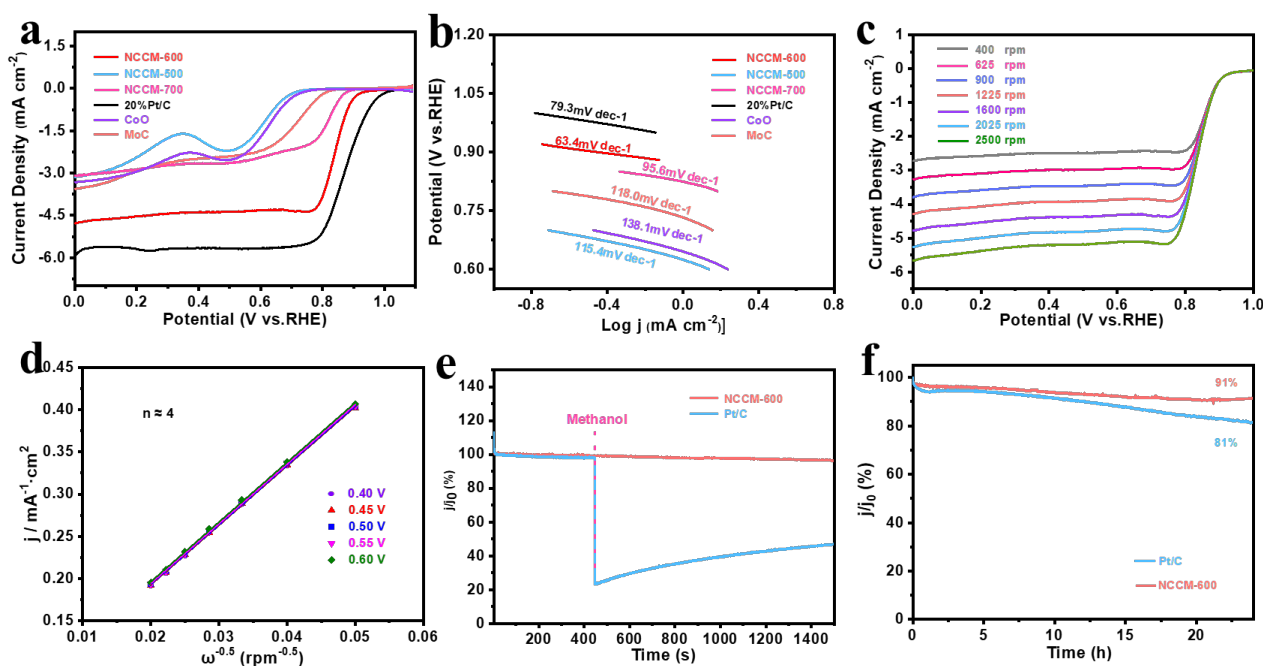


Figure 3. (a) LSV plots of the catalysts in the O₂-saturated alkaline electrolyte at 1600 rpm, (b) Tafel plots, (c) LSV curves of the NCCM-600 at different rotation rates, (d) K-L plots at different potentials, (e) durability evaluation of NCCM-600 and Pt/C electrodes at 0.6 V (vs. RHE) on addition of methanol, and (f) chronoamperometric responses acquired for ORR at NCCM-600 and Pt/C electrodes at 0.6 V (vs. RHE).

In addition, the electrocatalytic performance of the catalysts for oxygen evolution reaction (OER) was evaluated in a 1.0 mol/L KOH solution and compared with that of commercial RuO₂. Thanks to the interconnected heterojunction nanocrystals and N-doped porous C, NCCM-600 has a similar overpotential ($E_{10} = 0.348$ V) versus RuO₂ ($E_{10} = 0.341$ V), and the corresponding Tafel plots confirmed that NCCM-600 was lower (Figure S6a,b). The overpotential and Tafel confirm that the OER catalytic activity of NCCM-600 was better than RuO₂. The negligible overpotential loss of NCCM-600 is obtained after 26 h (Figure S6c), demonstrating the remarkable long-term stability and durability. Moreover, as depicted in Figure S7, electrochemical impedance spectroscopy (EIS) was performed to explain the lower charge-transfer resistance of NCCM-600 compared to MOF-derived CoO and MoC. The superior electrical conductivity may effectively enhance the electrocatalytic process. The electrochemical surface area (ECSA) of different catalysts was evaluated by testing the CVs of samples in a non-Faradaic potential range at various scan rates. The Cdl value is directly proportional to the ECSA. The significantly superior ECSA of NCCM-600 compared to CoO and MoC (Figure S8) indicates that NCCM-600 can expose more active sites, thus exhibiting better catalytic activity.

Furthermore, in order to demonstrate the outstanding ORR and OER catalytic performance of NCCM-600, a comparison was made between its ORR and OER catalytic performance and that of previously reported non-precious metal bifunctional electrocatalysts. The ORR catalytic activity was evaluated by measuring the half-wave potential ($E_{1/2}$), while the OER catalytic activity was assessed by measuring the overpotential (E_{10}). According to Table S1, NCCM-600 exhibits superior ORR catalytic performance and OER catalytic activity compared to most Co-based and Mo-based compounds reported as bifunctional electrocatalysts. The heterojunction structure plays a crucial role in optimizing the electronic structure of the catalyst, increasing its conductivity and active surface area, which are essential for improving electrocatalytic performance. These results clearly demonstrate the significantly improved multifunctional catalytic performance of NCCM-600 towards both ORR and OER.

A rechargeable Zn–air battery (ZAB) was assembled to demonstrate the practical potential of the MOF–derived N–doped porous C@CoO/MoC heterojunction composite. Figure 4a illustrates the schematic of the liquid ZAB, which employs a zinc plate as an anode and a carbon fiber paper coated with NCCM–600 as a cathode electrode. The NCCM–600–based ZAB exhibits an open–circuit voltage of 1.403 V (Figure 4b). As shown in Figure 4c, the peak power density of the NCCM–600–based ZAB is significantly higher at 133.36 mW/cm² compared to that of Pt/C–RuO₂ (122.59 mW/cm²). At a current density of 50 mA·cm^{−2}, the discharge and charge voltages of the NCCM–600 battery were measured at 1.124V and 2.127 V, respectively, which are similar to those observed for Pt/C+RuO₂–based ZABs (Figure S9). Additionally, the superior heterojunction catalyst provides a stable galvanostatic discharge property for ZAB. The NCCM–600–based ZAB possesses a higher specific capacity of 778.45 mAh/g compared to Pt/C+RuO₂–based ZAB with 747.38 mAh/g (normalized by the total mass of consumed Zn). Moreover, the NCCM–600–based ZAB exhibits exceptional cycling stability when repeatedly charged and discharged for more than 650 h (650 cycles, one cycle for 60 min) without any significant drop in overpotential (Figure 4e). This further demonstrates the high promise of MOF–derived N–doped porous C@CoO/MoC heterojunction composite for rechargeable ZAB applications.

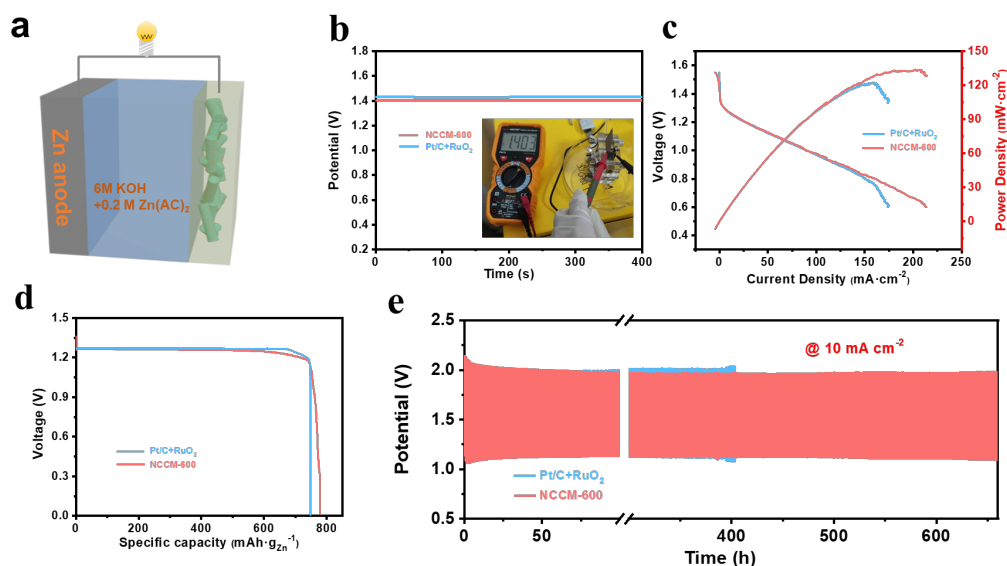


Figure 4. (a) Schematic illustration of configuration of the rechargeable ZAB using NCCM–600 as the air cathode, ZAB based on NCCM–600 and Pt/C+RuO₂ (b) Open–circuit voltage, (c) Power density curves, (d) Specific capacity normalized by the total mass of consumed Zn, (e) Discharge and charge voltage profiles at the current density of 10 mA cm^{−2}.

4. Conclusions

In summary, we have developed a facile strategy for the preparation of uniformly dispersed rod–like porous N–doped C–loaded CoO/MoC heterojunction bifunctional catalysts with high catalytic activity and stability. The optimal NCCM–600 catalyst exhibits impressive bifunctional electrocatalytic activity with a high–wave half potential ($E_{1/2} = 0.841$ V) for ORR and a low overpotential ($E_{10} = 348$ mV) for OER, accompanied by excellent stability. The exceptional practical applicability and electrocatalytic activity of the NCCM–600 catalyst are further revealed by its performance in a liquid ZAB. The constructed ZAB based on an NCCM–600 cathode achieves a peak power density of 133.36 mW cm^{−2} and a prolonged cycling life of more than 650 h. This synthetic strategy is particularly noteworthy as it significantly contributes to the expansion of nano/micro–structures in transition–metal–based heterostructure catalysts, thereby opening up avenues for developing functional materials with enhanced properties across a wide range of applications.

Supplementary Materials: The following supporting information can be downloaded at: <https://www.mdpi.com/article/10.3390/batteries9060306/s1>, Figure S1: (a) XRD patterns, (b) SEM images, and (c) EDX elemental mapping images of Co/Mo MOF; Figure S2: Full-survey XPS spectra of the CoO/MoC@N/C heterojunction composite; Figure S3: SEM images and XRD patterns of (a,b) Mo MOF-derived MoC and (c,d) Co MOF-derived CoO; Figure S4: Nitrogen adsorption-desorption isotherms and corresponding pore-size distribution of (a) NCCM-600, (b) Co MOF-derived CoO, and (c) Mo MOF-derived MoC; Figure S5: (a) CV curves of CoO/MoC@N/C heterojunction composite in 0.1 M KOH saturated with O₂ and N₂; Figure S6: (a) Linear sweep voltammetry (LSV) curves and (b) corresponding Tafel plots of NCCM-500, NCCM-600, NCCM-700, commercial RuO₂ and CoO (c) The stability of polarization curves of the NCCM-600; Figure S7: Nyquist plots of MOF-derived N-doped porous C@CoO/MoC heterojunction composite, MOF-derived MoC and MOF-derived CoO; Figure S8: CV curves of prepared (a) NCCM-600, (b) CoO, and (c) MoC in 1 M KOH at different scan rates. (b) Charging current density differences plotted against scan rate of the electrodes. The linear slope was used to represent the ECSA; Figure S9: Charge and discharge polarization curves of the fabricated Zn-air battery; Table S1: Comparison of the overpotentials for ORR (at E_{1/2}) and OER at (10 mA cm⁻²) of the prepared CoO/MoC@N/C heterojunction composite and other reported bifunctional electrocatalysts. References [52–62] are mentioned in the Supplementary Materials.

Author Contributions: Conceptualization, R.Y. and S.M.; methodology, S.M.; software, J.Y.; validation, R.Y., J.F. and Z.L.; formal analysis, X.N. and F.X.; investigation, R.Y.; resources, R.Y., W.L. and X.C.; data curation, S.M.; writing—original draft preparation, R.Y.; writing—review and editing, R.Y. and Y.Z.; visualization, X.C.; supervision, R.Y. and X.C.; project administration, S.M. and R.Y.; funding acquisition. All authors have read and agreed to the published version of the manuscript.

Funding: This research was funded by the National Natural Science Foundation of China (No. 51972286, 22005268, and 22275166), the Natural Science Foundation of Zhejiang Provincial Natural Science Foundation (LR19E020003 and LQ20B010011), the Foundation of the Zhejiang Provincial Educational Committee (GZ22453127001), the Fundamental Research Funds for the Provincial Universities of Zhejiang (RF B 2020004), and the Leading Innovative and Entrepreneur Team Introduction Program of Zhejiang (2020R01002).

Conflicts of Interest: The authors declare no conflict of interest.

References

1. Ling, Y.Y.; Ma, Q.L.; Yu, Y.F.; Zhang, B. Optimization Strategies for Selective CO₂ Electroreduction to Fuels. *Trans. Tianjin Univ.* **2021**, *27*, 180–200. [[CrossRef](#)]
2. Pan, J.; Xu, Y.Y.; Yang, H.; Dong, Z.; Liu, H.; Xia, B.Y. Advanced architectures and relatives of air electrodes in Zn-air batteries. *Adv. Sci.* **2018**, *5*, 1700691. [[CrossRef](#)]
3. O'donnell, L.F.; Greenbaum, S.G. Review of Multivalent Metal Ion Transport in Inorganic and Solid Polymer Electrolytes. *Batteries* **2021**, *7*, 3. [[CrossRef](#)]
4. Chen, H.; Zhang, S.; Liu, Q.; Yu, P.; Luo, J.; Hu, G.; Liu, X. CoSe₂ nanocrystals embedded into carbon framework as efficient bifunctional catalyst for alkaline seawater splitting. *Inorg. Chem. Commun.* **2022**, *146*, 110170. [[CrossRef](#)]
5. Liu, W.; Feng, J.; Wei, T.; Liu, Q.; Zhang, S.; Luo, Y.; Luo, J.; Liu, X. Active-site and interface engineering of cathode materials for aqueous Zn-gas batteries. *Nano Res.* **2022**, *16*, 2325–2346. [[CrossRef](#)]
6. Gao, S.; Wei, T.; Sun, J.; Liu, Q.; Ma, D.; Liu, W.; Zhang, S.; Luo, J.; Liu, X. Atomically Dispersed Metal-Based Catalysts for Zn-CO₂ Batteries. *Small Struct.* **2022**, *3*, 2200086. [[CrossRef](#)]
7. Zhang, H.; Luo, Y.; Chu, P.K.; Liu, Q.; Liu, X.; Zhang, S.; Luo, J.; Wang, X.; Hu, G. Recent advances in non-noble metal-based bifunctional electrocatalysts for overall seawater splitting. *J. Alloys Compd.* **2022**, *922*, 166113. [[CrossRef](#)]
8. Ding, J.; Yang, H.; Zhang, S.; Liu, Q.; Cao, H.; Luo, J.; Liu, X. Advances in the electrocatalytic hydrogen evolution reaction by metal nanoclusters-based materials. *Small* **2022**, *18*, 2204524. [[CrossRef](#)]
9. Lee, D.; Kim, H.-W.; Kim, J.-M.; Kim, K.-H.; Lee, S.-Y. Flexible/rechargeable Zn-air batteries based on multifunctional heteronanomaterial architecture. *ACS Appl. Mater. Interfaces* **2018**, *10*, 22210–22217. [[CrossRef](#)]
10. Chen, X.; Pu, J.; Hu, X.; An, L.; Jiang, J.; Li, Y. Confinement synthesis of bimetallic MOF-derived defect-rich nanofiber electrocatalysts for rechargeable Zn-air battery. *Nano Res.* **2022**, *15*, 9000–9009. [[CrossRef](#)]
11. Wang, Y.; Cao, Q.; Guan, C.; Cheng, C. Recent advances on self-supported arrayed bifunctional oxygen electrocatalysts for flexible solid-state Zn-air batteries. *Small* **2020**, *16*, 2002902. [[CrossRef](#)] [[PubMed](#)]

12. Wang, X.; Li, Y.; Jin, T.; Meng, J.; Jiao, L.; Zhu, M.; Chen, J. Electrospun thin-walled CuCo_2O_4 @C nanotubes as bifunctional oxygen electrocatalysts for rechargeable Zn–air batteries. *Nano Lett.* **2017**, *17*, 7989–7994. [[CrossRef](#)]
13. Liu, W.; Que, W.; Yin, R.; Dai, J.; Zheng, D.; Feng, J.; Xu, X.; Wu, F.; Shi, W.; Liu, X.; et al. Ferrum-molybdenum dual incorporated cobalt oxides as efficient bifunctional anti-corrosion electrocatalyst for seawater splitting. *Appl. Catal. B Environ.* **2023**, *328*, 122488. [[CrossRef](#)]
14. Ying, J.-P.; Zheng, D.; Meng, S.-B.; Yin, R.-L.; Dai, X.-J.; Feng, J.-X.; Wu, F.-F.; Shi, W.-H.; Cao, X.-H. Advanced design strategies for multi-dimensional structured carbon materials for high-performance Zn-air batteries. *N. Carbon Mater.* **2022**, *37*, 641–657. [[CrossRef](#)]
15. Tian, Y.; Xu, L.; Li, M.; Yuan, D.; Liu, X.; Qian, J.; Dou, Y.; Qiu, J.; Zhang, S. Interface engineering of CoS/CoO@N-doped graphene nanocomposite for high-performance rechargeable Zn–Air batteries. *Nano-Micro Lett.* **2021**, *13*, 3. [[CrossRef](#)]
16. Zhang, H.; Wei, T.; Qiu, Y.; Zhang, S.; Liu, Q.; Hu, G.; Luo, J.; Liu, X. Recent progress in metal phosphorous chalcogenides: Potential high-performance electrocatalysts. *Small* **2023**, *19*, 2207249. [[CrossRef](#)]
17. Gu, Y.; Yan, G.; Lian, Y.; Qi, P.; Mu, Q.; Zhang, C.; Deng, Z.; Peng, Y. MnIII-enriched $\alpha\text{-MnO}_2$ nanowires as efficient bifunctional oxygen catalysts for rechargeable Zn-air batteries. *Energy Storage Mater.* **2019**, *23*, 252–260. [[CrossRef](#)]
18. Yin, J.; Li, Y.; Lv, F.; Fan, Q.; Zhao, Y.-Q.; Zhang, Q.; Wang, W.; Cheng, F.; Xi, P.; Guo, S. NiO/CoN porous nanowires as efficient bifunctional catalysts for Zn–air batteries. *ACS Nano* **2017**, *11*, 2275–2283. [[CrossRef](#)]
19. Liu, P.; Ran, J.; Xia, B.; Xi, S.; Gao, D.; Wang, J. Bifunctional oxygen electrocatalyst of mesoporous Ni/NiO nanosheets for flexible rechargeable Zn–Air batteries. *Nano-Micro Lett.* **2020**, *12*, 68. [[CrossRef](#)]
20. Tan, J.; Thomas, T.; Liu, J.; Yang, L.; Pan, L.; Cao, R.; Shen, H.; Wang, J.; Liu, J.; Yang, M. Rapid microwave-assisted preparation of high-performance bifunctional $\text{Ni}_3\text{Fe}/\text{Co-NC}$ for rechargeable Zn-air battery. *Chem. Eng. J.* **2020**, *395*, 125151. [[CrossRef](#)]
21. Hu, G.; Zou, G.; Qiao, M.; Wågberg, T.; Mamat, X.; Hu, X.; Wa, Y. Ni–Co bimetallic coordination effect for long lifetime rechargeable Zn–air battery. *J. Energy Chem.* **2020**, *47*, 146–154.
22. Luo, J.; Liu, Q.; Zhang, S.; Wei, T.; Liu, W.; Liu, X. A dual-functional Bi-doped Co_3O_4 nanosheets array towards high efficiency 5-hydroxymethylfurfural oxidation and hydrogen production. *Chem. Commun.* **2023**, *59*, 442–445.
23. Chen, G.; Xu, Y.; Huang, L.; Douka, A.I.; Xia, B.Y. Continuous nitrogen-doped carbon nanotube matrix for boosting oxygen electrocatalysis in rechargeable Zn-air batteries. *J. Energy Chem.* **2021**, *55*, 183–189. [[CrossRef](#)]
24. Chen, X.; Zhong, C.; Liu, B.; Liu, Z.; Bi, X.; Zhao, N.; Han, X.; Deng, Y.; Lu, J.; Hu, W. Atomic layer Co_3O_4 nanosheets: The key to knittable Zn–air batteries. *Small* **2018**, *14*, 1702987. [[CrossRef](#)]
25. Chen, X.; Pu, J.; Hu, X.; Yao, Y.; Dou, Y.; Jiang, J.; Zhang, W. Hollow nanofiber with bifunctional oxygen electrocatalyst for rechargeable Zn–Air battery. *Small* **2022**, *18*, 2200578. [[CrossRef](#)]
26. Xu, X.; Shi, W.; Liu, W.; Ye, S.; Yin, R.; Zhang, L.; Xu, L.; Chen, M.; Zhong, M.; Cao, X. Preparation of two-dimensional assembled Ni–Mn–C ternary composites for high-performance all-solid-state flexible supercapacitors. *J. Mater. Chem. A* **2018**, *6*, 24086–24091. [[CrossRef](#)]
27. Yuan, R.; Bi, W.; Zhou, T.; Zhang, N.; Zhong, C.; Chu, W.; Yan, W.; Xu, Q.; Wu, C.; Xie, Y. Two-dimensional hierarchical Fe–N–C electrocatalyst for Zn–Air batteries with ultrahigh specific capacity. *ACS Mater. Lett.* **2019**, *2*, 35–41. [[CrossRef](#)]
28. Meng, G.; Jin, M.; Wei, T.; Liu, Q.; Zhang, S.; Peng, X.; Luo, J. MoC nanocrystals confined in N-doped carbon nanosheets toward highly selective electrocatalytic nitric oxide reduction to ammonia. *Nano Res.* **2022**, *15*, 8890–8896. [[CrossRef](#)]
29. Liu, W.; Feng, J.; Yin, R.; Ni, Y.; Zheng, D.; Que, W.; Niu, X.; Dai, X.; Shi, W.; Wu, F.; et al. Tailoring oxygenated groups of monolithic cobalt-nitrogen-carbon frameworks for highly efficient hydrogen peroxide production in acidic media. *Chem. Eng. J.* **2022**, *430*, 132990. [[CrossRef](#)]
30. Liu, Y.T.; Chen, X.; Yu, J.; Ding, B. Carbon-nanoplated $\text{CoS}@ \text{TiO}_2$ nanofibrous membrane: An interface-engineered heterojunction for high-efficiency electrocatalytic nitrogen reduction. *Angew. Chem. Int. Ed.* **2019**, *131*, 19079–19083. [[CrossRef](#)]
31. Luo, M.; Sun, W.; Xu, B.; Pan, H.; Jiang, Y. Interface engineering of air electrocatalysts for rechargeable zinc–air batteries. *Adv. Energy Mater.* **2021**, *11*, 2002762. [[CrossRef](#)]
32. Zong, L.; Wu, W.; Liu, S.; Yin, H.; Chen, Y.; Liu, C.; Fan, K.; Zhao, X.; Chen, X.; Wang, F.; et al. Metal-free, active nitrogen-enriched, efficient bifunctional oxygen electrocatalyst for ultrastable zinc-air batteries. *Energy Storage Mater.* **2020**, *27*, 514–521. [[CrossRef](#)]
33. Xu, W.; Yoon, D.; Yang, Y.; Xiong, Y.; Li, H.; Zeng, R.; Muller, D.A.; Abruña, H.D. MOF-derived bimetallic Pd–Co alkaline ORR electrocatalysts. *ACS Appl. Mater. Interfaces* **2022**, *14*, 44735–44744. [[CrossRef](#)] [[PubMed](#)]
34. Luo, H.; Jiang, W.-J.; Niu, S.; Zhang, X.; Zhang, Y.; Yuan, L.-P.; He, C.; Hu, J.-S. Self-catalyzed growth of Co–N–C nanobrushes for efficient rechargeable Zn–Air Batteries. *Small* **2020**, *16*, 2001171. [[CrossRef](#)]
35. Cai, X.; Lai, L.; Lin, J.; Shen, Z. Recent advances in air electrodes for Zn–air batteries: Electrocatalysis and structural design. *Mater. Horiz.* **2017**, *4*, 945–976. [[CrossRef](#)]
36. Wang, H.F.; Tang, C.; Wang, B.; Li, B.-Q.; Zhang, Q. Bifunctional transition metal hydroxysulfides: Room-temperature sulfurization and their applications in Zn–air batteries. *Adv. Mater.* **2017**, *29*, 1702327. [[CrossRef](#)]
37. Liu, W.; Yin, R.; Xu, X.; Zhang, L.; Shi, W.; Cao, X. Structural engineering of low-dimensional metal–organic frameworks: Synthesis, properties, and applications. *Adv. Sci.* **2019**, *6*, 1802373. [[CrossRef](#)]

38. Yang, X.G.; Sun, X.; Gan, L.; Sun, L.; Mi, H.; Zhang, P.; Ren, X.; Li, Y. A CoOx/FeOx heterojunction on carbon nanotubes prepared by plasma-enhanced atomic layer deposition for the highly efficient electrocatalysis of oxygen evolution reactions. *J. Mater. Chem. A* **2020**, *8*, 15140–15147. [[CrossRef](#)]
39. Huang, C.; Miao, X.; Pi, C.; Gao, B.; Zhang, X.; Qin, P.; Huo, K.; Peng, X.; Chu, P.K. Mo₂C/VC heterojunction embedded in graphitic carbon network: An advanced electrocatalyst for hydrogen evolution. *Nano Energy* **2019**, *60*, 520–526. [[CrossRef](#)]
40. Liu, W.; Yu, L.; Yin, R.; Xu, X.; Feng, J.; Jiang, X.; Zheng, D.; Gao, X.; Gao, X.; Que, W.; et al. Non-3d metal modulation of a 2D Ni–Co heterostructure array as multifunctional electrocatalyst for portable overall water splitting. *Small* **2020**, *16*, 1906775. [[CrossRef](#)]
41. Liu, W.; Yin, R.; Shi, W.; Xu, X.; Shen, X.; Yin, Q.; Xu, L.; Cao, X. Gram-scale preparation of 2D transition metal hydroxide/oxide assembled structures for oxygen evolution and Zn-air battery. *ACS Appl. Energy Mater.* **2018**, *2*, 579–586. [[CrossRef](#)]
42. Liu, W.; Zheng, D.; Zhang, L.; Yin, R.; Xu, X.; Shi, W.; Wu, F.; Cao, X.; Lu, X. Bioinspired interfacial engineering of a CoSe₂ decorated carbon framework cathode towards temperature-tolerant and flexible Zn–air batteries. *Nanoscale* **2021**, *13*, 3019–3026. [[CrossRef](#)]
43. Wu, F.-F.; Gao, X.; Xu, X.; Jiang, Y.; Gao, X.; Yin, R.; Shi, W.; Liu, W.; Lu, G.; Cao, X. MnO₂ nanosheet-assembled hollow polyhedron grown on carbon cloth for flexible aqueous zinc-ion batteries. *ChemSusChem* **2020**, *13*, 1537–1545. [[CrossRef](#)] [[PubMed](#)]
44. Cao, X.; Tan, C.; Sindoro, M.; Zhang, H. Correction: Hybrid micro-/nano-structures derived from metal–organic frameworks: Preparation and applications in energy storage and conversion. *Chem. Soc. Rev.* **2018**, *47*, 5997. [[CrossRef](#)] [[PubMed](#)]
45. Guan, Y.; Nan, L.; He, J.; Li, Y.; Zhang, L.; Zhang, Q.; Ren, X.; He, C.; Zheng, L.; Sun, X. Tuning and understanding the electronic effect of Co–Mo–O sites in bifunctional electrocatalysts for ultralong-lasting rechargeable Zinc-air batteries. *J. Mater. Chem. A* **2021**, *9*, 21716–21722. [[CrossRef](#)]
46. Cao, X.; Tan, C.; Zhang, X.; Zhao, W.; Zhang, H. Solution-processed two-dimensional metal dichalcogenide-based nanomaterials for energy storage and conversion. *Adv. Mater.* **2016**, *28*, 6167–6196. [[CrossRef](#)]
47. Lim, J.; Jung, J.-W.; Kim, N.-Y.; Lee, G.Y.; Lee, H.J.; Lee, Y.; Choi, D.S.; Yoon, K.R.; Kim, Y.-H.; Kim, I.-D.; et al. N₂-dopant of graphene with electrochemically switchable bifunctional ORR/OER catalysis for Zn-air battery. *Energy Storage Mater.* **2020**, *32*, 517–524. [[CrossRef](#)]
48. Amiin, I.S.; Pu, Z.; Liu, X.; Owusu, K.A.; Monestel, H.G.R.; Boakye, F.O.; Zhang, H.; Mu, S. Multifunctional Mo–N/C@ MoS₂ electrocatalysts for HER, OER, ORR, and Zn–air batteries. *Adv. Funct. Mater.* **2017**, *27*, 1702300. [[CrossRef](#)]
49. He, B.; Wang, J.; Fan, Y.; Jiang, Y.; Zhai, Y.; Wang, Y.; Huang, Q.; Dang, F.; Zhang, Z.; Wang, N. Mesoporous CoO/Co–N–C nanofibers as efficient cathode catalysts for Li–O₂ batteries. *J. Mater. Chem. A* **2018**, *6*, 19075–19084. [[CrossRef](#)]
50. Zhou, X.; Tian, Y.; Luo, J.; Jin, B.; Wu, Z.; Ning, X.; Zhan, L.; Fan, X.; Zhou, T.; Zhang, S.; et al. MoC Quantum Dots@ N-Doped-Carbon for Low-Cost and Efficient Hydrogen Evolution Reaction: From Electrocatalysis to Photocatalysis. *Adv. Funct. Mater.* **2022**, *32*, 2201518. [[CrossRef](#)]
51. Zhang, L.; Zhu, Y.; Nie, Z.; Li, Z.; Ye, Y.; Li, L.; Hong, J.; Bi, Z.; Zhou, Y.; Hu, G. Co/MoC nanoparticles embedded in carbon nanoboxes as robust trifunctional electrocatalysts for a Zn–air battery and water electrocatalysis. *ACS Nano* **2021**, *15*, 13399–13414. [[CrossRef](#)]
52. Chou, S.C.; Tso, K.C.; Hsieh, Y.C.; Sun, B.Y.; Lee, J.F.; Wu, P.W. Facile synthesis of Co₃O₄@ CoO@ Co gradient core@ shell nanoparticles and their applications for oxygen evolution and reduction in alkaline electrolytes. *Materials* **2020**, *13*, 2703. [[CrossRef](#)]
53. Jin, W.; Chen, J.; Liu, B.; Hu, J.; Wu, Z.; Cai, W.; Fu, G. Oxygen Vacancy–Rich In-Doped CoO/CoP Heterostructure as an Effective Air Cathode for Rechargeable Zn–Air Batteries. *Small* **2019**, *15*, 1904210. [[CrossRef](#)]
54. Chen, S.; Chen, S.; Zhang, B.; Zhang, J. Bifunctional oxygen electrocatalysis of N, S-codoped porous carbon with interspersed hollow CoO nanoparticles for rechargeable Zn–air batteries. *ACS Appl. Mater. Interfaces* **2019**, *11*, 16720–16728. [[CrossRef](#)]
55. Guo, C.; Zheng, Y.; Ran, J.; Xie, F.; Jaroniec, M.; Qiao, S.Z. Engineering high-energy interfacial structures for high-performance oxygen-involving electrocatalysis. *Angew. Chem. Int. Ed.* **2017**, *56*, 8539–8543. [[CrossRef](#)] [[PubMed](#)]
56. Zhang, M.; Han, C.; Cao, W.Q.; Cao, M.S.; Yang, H.J.; Yuan, J. A nano-micro engineering nanofiber for electromagnetic absorber, green shielding and sensor. *Nano-Micro Lett.* **2021**, *13*, 1–12. [[CrossRef](#)]
57. Defo, C.; Mishra, A.K.; Yerima, B.P.K.; Mabou, P.B.; Ako, A.A.; Fonkou, T. Current conditions of groundwater resources development and related problems in the Republic of Cameroon, West Africa. *Eur. Water* **2016**, *54*, 43–68.
58. Zhao, Y.; Lai, Q.; Zhu, J.; Zhong, J.; Tang, Z.; Luo, Y.; Liang, Y. Controllable construction of core–shell polymer@ zeolitic imidazolate frameworks fiber derived heteroatom-doped carbon nanofiber network for efficient oxygen electrocatalysis. *Small* **2018**, *14*, 1704207. [[CrossRef](#)] [[PubMed](#)]
59. Tomon, C.; Sarawutanukul, S.; Duangdangchote, S.; Krittayavathananon, A.; Sawangphruk, M. Photoactive Zn–air batteries using spinel-type cobalt oxide as a bifunctional photocatalyst at the air cathode. *Chem. Commun.* **2019**, *55*, 5855–5858. [[CrossRef](#)] [[PubMed](#)]
60. Sadighi, Z.; Liu, J.; Zhao, L.; Ciucci, F.; Kim, J.K. Metallic MoS₂ nanosheets: Multifunctional electrocatalyst for the ORR, OER and Li–O₂ batteries. *Nanoscale* **2018**, *10*, 22549–22559. [[CrossRef](#)] [[PubMed](#)]

61. Ouyang, B.; Artrith, N.; Lun, Z.; Jadidi, Z.; Kitchaev, D.A.; Ji, H.; Urban, A.; Ceder, G. Effect of Fluorination on Lithium Transport and Short-Range Order in Disordered-Rocksalt-Type Lithium-Ion Battery Cathodes. *Adv. Energy Mater.* **2020**, *10*, 1903240. [[CrossRef](#)]
62. Liu, H.; Liu, Y.; Mehdi, S.; Wu, X.; Liu, T.; Zhou, B.; Zhang, P.; Jiang, J.; Li, B. Surface Phosphorus-Induced CoO Coupling to Monolithic Carbon for Efficient Air Electrode of Quasi-Solid-State Zn-Air Batteries. *Adv. Sci.* **2021**, *8*, 2101314. [[CrossRef](#)] [[PubMed](#)]

Disclaimer/Publisher's Note: The statements, opinions and data contained in all publications are solely those of the individual author(s) and contributor(s) and not of MDPI and/or the editor(s). MDPI and/or the editor(s) disclaim responsibility for any injury to people or property resulting from any ideas, methods, instructions or products referred to in the content.